



HAL
open science

Assessment of FGPM shunt damping for vibration reduction of laminated composite beams

M. Lezgy-Nazargah, S. M. Divandar, Philippe Vidal, Olivier Polit

► **To cite this version:**

M. Lezgy-Nazargah, S. M. Divandar, Philippe Vidal, Olivier Polit. Assessment of FGPM shunt damping for vibration reduction of laminated composite beams. *Journal of Sound and Vibration*, 2017, 389, pp.101-118. 10.1016/j.jsv.2016.11.023 . hal-01676248

HAL Id: hal-01676248

<https://hal.parisnanterre.fr/hal-01676248>

Submitted on 5 Jan 2018

HAL is a multi-disciplinary open access archive for the deposit and dissemination of scientific research documents, whether they are published or not. The documents may come from teaching and research institutions in France or abroad, or from public or private research centers.

L'archive ouverte pluridisciplinaire **HAL**, est destinée au dépôt et à la diffusion de documents scientifiques de niveau recherche, publiés ou non, émanant des établissements d'enseignement et de recherche français ou étrangers, des laboratoires publics ou privés.

Assessment of FGPM shunt damping for vibration reduction of laminated composite beams

M. Lezgy-Nazargah, S.M. Divandar, P. Vidal, O. Polit

ABSTRACT

This work addresses theoretical and finite element investigations of functionally graded piezoelectric materials (FGPMs) for shunted passive vibration damping of laminated composite beams. The properties of piezoelectric patches are assumed to vary through the thickness direction following the exponent or power law distribution in terms of the volume fractions of the constituent materials. By employing Hamilton's principle, the governing differential equations of motion are derived. The resulting system of equations of vibration is solved by employing an efficient three-noded beam element which is based on a refined sinus piezoelectric model. The effects of effective electromechanical coupling coefficients (EEMCCs), different electric shunt circuits and different material compositions on the shunted damping performance are investigated. The optimal values of the electric components belonging to each shunt circuit are numerically determined.

1. Introduction

Piezoelectric material can convert electrical energy into mechanical energy and vice-versa. It is nowadays widely used for both active and passive vibration control of flexible structures. In active control, a structure is provided with a set of piezoelectric patches as sensors for detecting the vibration and some piezoelectric patches as actuators for changing the structural response of the system. These piezoelectric sensors and actuators are coupled together by a controller to suitably analyze the voltage signals from the piezoelectric sensors and reduce the undesired vibrations of the structure by applying the appropriate voltage to the actuators [1]. Active control not only requires high-voltage amplifiers to drive the piezoelectric actuators, but also exhibit instability due to spillover effects [2] of uncontrolled eigenmodes of the vibrating structure. The passive control is achieved by shunting the suitable electric circuits to piezoelectric patches bonded to the vibrating structure. Piezoelectric patches transform the mechanical vibration energy to electrical energy [3]. The transformed electrical energy can be dissipated into heat energy by shunt electric circuits. Piezoelectric patches shunted with passive electrical networks can be attached to a host structure for reduction of structural vibrations. In contrast to active control, this approach guarantees the stability of the system. Moreover, the later approach has low complexity in implementation.

The passive vibration control via piezoelectric materials which is frequently called "shunted piezoelectric damping", was firstly presented by Hagood and Flotow [4]. Due to its simplicity, lightness, and small size, the shunted piezoelectric

technique has been widely studied by many researchers. Becker et al. [5] presented a finite element formulation for numerical treatment of shunted damped structures. In the finite element formulation of these researchers, the piezoelectric coupling effects of the patches as well as the electrical dynamics of the connected passive electrical circuits are incorporated. In this reference, the damping ratios are determined from the eigenvalue problem corresponding to the coupled model containing piezoelectric structure and passive electrical circuit. The effects of parameters like the passive electrical network and the variation of the patch thickness on modal damping ratios have been studied by these researchers. Ducarne et al. [6] introduced a strategy for placement and dimension optimization of shunted piezoelectric patches for vibration reduction. The procedure of these researchers is based on the maximization of the modal electro-mechanical coupling factor of the mechanical vibration mode to which the shunt is tuned. Thomas et al. [7] investigated the passive reduction of structural vibration by means of two classical resistive and resonant shunted piezoelectric patches. They proposed closed-form solutions to systematically estimate the performances of the piezoelectric shunts in the attenuation of free and forced vibrations of the elastic host structures. Caruso [8] analyzed and compared the vibration shunted damping performance of elastic structures considering three different electric circuits. He also determined the optimal values of the electric components belonging to each shunt circuit, taking into account the inherent structural damping of host vibrating structures. Park et al. [9] studied the vibration control of plates with shunted piezoelectric dampers. In this reference, the governing equations of motion are derived by employing the classical laminate plate theory and Hamilton's principle. Park et al. validated their theoretical formulation experimentally for simply supported aluminum plates. Delpero et al. [10] proposed a robust method for the measurement and prediction of loss factor in the piezoelectric shunted damping. The method of these researchers is based on the analysis of the dynamic response of the structure when the piezoelectric patches are connected to a resonant shunt circuit. Vasques [11] improved the passive shunt damping performance of a two-layered resonant-shunted piezo-elastic smart beam structure using modal piezoelectric transducers with shaped electrodes. They employed a one-dimensional coupled electromechanical analytical model based on equivalent single-layer Euler-Bernoulli beam model to design modal and uniform electrodes of piezoelectric transducers. Alaimo et al. [12] presented a one-dimensional finite element method for active and passive vibration damping of layered piezoelectric beams. The model of these researchers is based on the first-order shear deformation beam theory. In order to express the problem in terms of the mechanical variables, Aliamo and colleagues employed a preliminary analytical condensation of the electric state to the mechanical state. In this reference, the finite element model has been formulated in the frame of state-space approach and its efficiency has been evaluated for both active and passive vibration damping problems. Larbi et al. [13] used the piezoelectric elements connected with resonant shunt circuits, for the vibration damping of some specific resonance frequencies of the double laminated panels with viscoelastic core. Taking into account the frequency dependence of the viscoelastic material, they proposed a finite element formulation for the fully coupled visco-electro-mechanical-acoustic system. To solve the problem at a lower cost, Larbi and colleagues used a modal reduction approach. Park and Han [14] studied the sensitivities of damping performance with respect to system parameters for three types of passive shunted piezoelectric. They selected a loss factor as a performance index for the damping performance of each type of shunted piezoelectric. They also evaluated the damping performance degradation varying temperature conditions. Behrens et al. [15] introduced a current flowing controller as an alternative method for multiple mode piezoelectric shunt damping. The proposed piezoelectric shunt circuit which requires less resistors, capacitors and inductors, can also damp multiple modes using a single piezoelectric transducer.

In order to achieve higher shunted piezoelectric damping performances, the piezoelectric patches should be made of several layers of different piezoelectric materials. Although this conventional type of design may provide higher damping performances, it has several disadvantages. In these types of piezoelectric transducers, adhesive epoxy resin is usually used to bond the piezoelectric layers, which causes high stress concentrations at the layer interfaces. These stress concentrations lead to the initiation and propagation of micro-cracks near the interfaces of two bonded piezoelectric layers. Such drawbacks reduce lifetime and reliability of these structures. The main drawbacks of the conventional piezoelectric transducers can be overcome by using FGPMs. FGPMs are a kind of piezoelectric materials whose mechanical and electrical properties vary continuously in one or more directions [16]. The aim of this paper is to evaluate the performance of shunted FGPM damping for vibration control of laminated composite beams. A refined Sinus beam finite element is employed for static, free vibration and transient dynamic response of FGPM beams. To this end, the governing differential equations of motion are firstly derived using Hamilton's principle. The resulting system of equations are also reorganized to take into account the addition of the shunted piezoelectric configurations. A simple finite element model is used for solving the governing equations. The proposed beam element is a three-noded element which satisfies the continuity conditions between layers for displacements, transverse shear stress and the free conditions at the top and bottom surfaces of the beam. Moreover, the computational cost of the present element is very low in comparison with the available layer-wise beam and plate/shell theories. It has four independent generalized displacements. The employed element is based on the Sinus model kinematics introduced in Touratier [17]. Then, it has been extended to take into account the interlaminar continuity of the transverse shear stresses in Polit and Touratier [18] for plates, and in Dau et al [19] for shells. The coupling with the piezoelectric effect is carried out in Ossadzow-David and Touratier [20], and Fernandes and Pouget [21] using an analytical approach. The original Sinus model has been enriched in Vidal and Polit [22] by introducing a layer refinement in the kinematics, and then extended to thermal (Vidal and Polit [23]) and piezoelectric ([16,24]) effects. In the present study, it is intended to extend these last works to FGPM shunt damping of laminated composite beams. It is assumed that all material properties of FGPM transducers are variable along the thickness direction. Through the numerical examples, the effects of the Effective

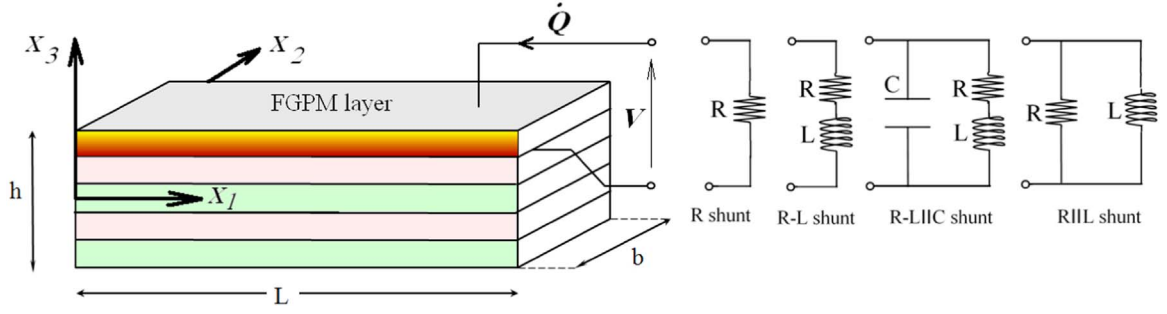


Fig. 1. Geometry of laminated beam passively controlled by the different FGPM shunt circuits.

Electromechanical Coupling Coefficients (EEMCCs), electric shunt circuits and material gradient composition of FGPM transducers on the shunted damping performance are assessed and discussed. The optimal values of the electric components belonging to each shunt circuit are numerically determined. Various results are presented in order to validate and illustrate the efficiency of the proposed refined Sinus finite element model. The damping performance of the shunted FGPM is investigated and assessed for different electric circuits connected to electrodes.

2. Mathematical formulations

2.1. Basic equations

The laminated beam of the present study has a rectangular uniform cross section of length L , width b , height h , and is made of N_l layers either completely or in part constituted of electroded FGPMs. The FGPM layers of the laminated beam are poled along the thickness direction (x_3) with an electrical field applied parallel to this polarization. As shown in Fig. 1, four different circuits are shunted to the FGPM layers: R shunt, R-L shunt, R-LIIC shunt and RIIL shunt. In this figure, V denotes the voltage between the electrodes and Q is the electric charge in one of the electrodes. The overhead dot denotes the differentiation with respect to time. R , L and C denote the value of resistance, inductance and external capacity of the shunt circuit, respectively. The considered Cartesian coordinate system is shown in Fig. 2.

In a smart laminated beam with small width, the following assumptions are made:

$$\sigma_{22}^{(k)} \cong 0, \quad \sigma_{33}^{(k)} \cong 0, \quad \sigma_{12}^{(k)} \cong 0, \quad \sigma_{23}^{(k)} \cong 0, \quad E_2^{(k)} \cong 0 \quad (1)$$

Using the conditions (1), the reduced linear constitutive equations of the k th FGPM layer can be written as

$$\begin{Bmatrix} \boldsymbol{\sigma}^{(k)} \\ \boldsymbol{D}^{(k)} \end{Bmatrix} = \begin{bmatrix} \bar{\boldsymbol{c}}^{(k)} & -\bar{\boldsymbol{e}}^{(k)} \\ \bar{\boldsymbol{e}}^{(k)} & \bar{\boldsymbol{\chi}}^{(k)} \end{bmatrix} \begin{Bmatrix} \boldsymbol{\epsilon}^{(k)} \\ \boldsymbol{E}^{(k)} \end{Bmatrix} \quad (2)$$

where $\boldsymbol{\sigma}^{(k)} = \{\sigma_{11}^{(k)} \ \sigma_{13}^{(k)}\}^T$ is the elastic stress vector and $\boldsymbol{\epsilon}^{(k)} = \{\epsilon_{11}^{(k)} \ \gamma_{13}^{(k)}\}^T$ the elastic strain vector, $\boldsymbol{E}^{(k)} = \{E_3^{(k)}\}$ the electric field vector and $\boldsymbol{D}^{(k)} = \{D_3^{(k)}\}$ is the electric displacement vector. $\bar{\boldsymbol{c}}^{(k)}$, $\bar{\boldsymbol{e}}^{(k)}$ and $\bar{\boldsymbol{\chi}}^{(k)}$ are the reduced elastic constitutive matrix, the piezoelectric matrix and the dielectric matrix, respectively. The elements of the aforementioned matrices can be calculated using static condensation procedure detailed in [24]. Unlike the homogeneous piezoelectric materials, elements of matrices $\bar{\boldsymbol{c}}^{(k)}$, $\bar{\boldsymbol{e}}^{(k)}$ and $\bar{\boldsymbol{\chi}}^{(k)}$ appeared in Eq. (2) are not constant values in the thickness direction. They are functions of the coordinate x_3 and vary according to the power law, exponent law or every other arbitrary distribution along the thickness direction of FGPM layers.

The displacement field used for smart laminated beam is based on Refined sinus model [16]:

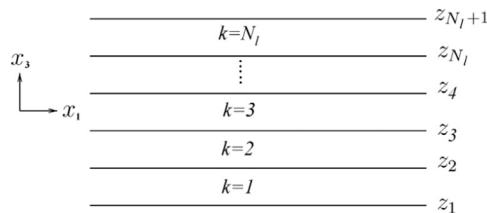


Fig. 2. Cartesian coordinate system of laminated smart beam.

$$\begin{aligned} u_1(x_1, x_2, x_3, t) &= u_0(x_1, t) - x_3 w(x_1, t)_{,1} + F(x_3)(\omega_3(x_1, t) + w(x_1, t)_{,1}) + S(x_3) u_{31}^1(x_1, t) \\ u_3(x_1, x_2, x_3, t) &= w_0(x_1, t) \end{aligned} \quad (3)$$

where the functions $u_1(x_1, x_2, x_3, t)$ and $u_3(x_1, x_2, x_3, t)$ represent the axial and transverse displacement components, respectively. $u_0(x_1, t)$ and $w_0(x_1, t)$ are the displacement components of the central line. t is the time and $\omega_3(x_1, t)$ denotes the shear-bending rotation around the x_2 axis. $u_{31}^1(x_1, t)$ is a supplementary unknown function associated with the refinement per layer. The comma denotes partial differentiation with respect to the coordinate x_i . The expression for $F(x_3)$ and $S(x_3)$ can be found in Ref. [16]. It is seen from Eq. (3) that the refined sinus model includes only four mechanical generalized unknowns u_0 , w_0 , ω_3 and u_{31}^1 .

In this study, a linear electric potential is assumed along the thickness direction of the FGPM layers. The electric field of the k th FGPM layer is given by:

$$\mathbf{E}^{(k)} = \{E_3^{(k)}\} = -V_{,3}^{(k)} = -(1/h^{(k)}) V^{(k)} \quad (4)$$

where $h^{(k)}$ is the thickness and $V^{(k)}$ is the electric potential difference acting on the k -th piezoelectric layer.

2.2. The system to be solved

The principle of virtual work for the piezoelectric medium of volume Ω and regular boundary surface Γ can be written as:

$$\begin{aligned} \delta\Pi = \delta U - \delta W = & - \int_{\Omega} \delta \boldsymbol{\varepsilon}^T \boldsymbol{\sigma} d\Omega + \int_{\Gamma} \delta \mathbf{u}^T \mathbf{F}_S d\Gamma + \int_{\Omega} \delta \mathbf{u}^T \mathbf{F}_V d\Omega - \int_{\Omega} \rho \delta \mathbf{u}^T \ddot{\mathbf{u}} d\Omega \\ & + \int_{\Omega} \delta \mathbf{E}^T \mathbf{D} d\Omega - \int_{\Gamma} \bar{Q} \delta \boldsymbol{\varphi} d\Gamma - \int_{\Omega} \bar{q} \delta \boldsymbol{\varphi} d\Omega = 0 \end{aligned} \quad (5)$$

where \mathbf{F}_S , \mathbf{F}_V , \bar{q} , \bar{Q} and ρ are surface force vector, mechanical body force vector, electrical body charge, surface charge and mass density, respectively. $\delta \mathbf{u}$ and $\delta \boldsymbol{\varphi}$ are admissible virtual displacement and potential.

2.3. Finite element application

In this section, finite element approximations are defined for the mechanical and electrical variables introduced in Section 2.1. The transverse deflection w_0 is interpolated using the C^1 -continuous Hermite cubic shape functions while Lagrangian quadratic shape functions are used for the interpolation of ω_3 , u_0 and u_{31}^1 . Due to the presence of the electrodes on the top and bottom surfaces of FGPM layers (equipotential condition), $V^{(k)}$ is considered to be constant in each element. The developed beam element has three nodes with a variable number of electric potential degrees of freedom on each element. Indeed, the number of electric potential degrees of freedom at each element is dependent on the number of FGPM layers. The electric potential, displacements, strain and electric field components may be expressed in terms of the mechanical and electrical degrees of freedom as follows:

$$\begin{bmatrix} \mathbf{u} \\ \boldsymbol{\varphi} \end{bmatrix} = \begin{bmatrix} \mathbf{N}_{uu} & \mathbf{0} \\ \mathbf{0} & \mathbf{N}_{\varphi\varphi} \end{bmatrix} \begin{bmatrix} \hat{\mathbf{u}}_u^e \\ \hat{\boldsymbol{\varphi}}^e \end{bmatrix}, \quad \begin{bmatrix} \boldsymbol{\varepsilon} \\ \mathbf{E} \end{bmatrix} = \begin{bmatrix} \mathbf{B}_{uu} & \mathbf{0} \\ \mathbf{0} & \mathbf{B}_{\varphi\varphi} \end{bmatrix} \begin{bmatrix} \hat{\mathbf{u}}_u^e \\ \hat{\boldsymbol{\varphi}}^e \end{bmatrix} \quad (6)$$

where $\mathbf{u} = [u_1 \ u_3]^T$, $\boldsymbol{\varphi} = [V^{(k)}]^T$, $\boldsymbol{\varepsilon} = [\varepsilon_{11} \ \gamma_{13}]^T$, $\mathbf{E} = [E_3]^T$, $\hat{\boldsymbol{\varphi}}^e = \left\{ \underbrace{V_1^{(k)} \ V_2^{(k)} \ \dots \ V_n^{(k)}}_{\text{the number of electrodes}} \right\}$, and

$$\hat{\mathbf{u}}_u^e = \left\{ (u_0)_1 \ (w_0)_1 \ (\omega_3)_1 \ (w_{0,1})_1 \ (u_{31}^1)_1; (u_0)_3 \ (\omega_3)_3 \ (u_{31}^1)_3; (u_0)_2 \ (w_0)_2 \ (\omega_3)_2 \ (w_{0,1})_2 \ (u_{31}^1)_2 \right\}^T$$

For sake of brevity, the elements of matrices \mathbf{N}_{uu} , $\mathbf{N}_{\varphi\varphi}$, \mathbf{B}_{uu} and $\mathbf{B}_{\varphi\varphi}$ are not presented here. For further details on the FE formulations, the interested readers can refer to [16].

Substituting Eqs. (2) and (6) into Eq. (5), and assembling the elementary matrices yield the following classical general dynamic of motion:

$$\mathbf{M}_{uu} \hat{\mathbf{u}}(t) + \mathbf{K}_{uu} \hat{\mathbf{u}}(t) + \mathbf{K}_{u\varphi} \hat{\boldsymbol{\varphi}}(t) = \mathbf{F}(t) \quad (7.a)$$

$$\mathbf{K}_{\varphi u} \hat{\mathbf{u}}(t) + \mathbf{K}_{\varphi\varphi} \hat{\boldsymbol{\varphi}}(t) = \mathbf{Q}(t) \quad (7.b)$$

The matrices and vectors in the above equations are the mechanical degrees of freedom $\hat{\mathbf{u}}(t)$, the electrical degrees of freedom $\hat{\boldsymbol{\varphi}}(t)$, the mass matrix $\mathbf{M}_{uu} = \int_{\Omega} \rho \mathbf{N}_{uu}^T \mathbf{N}_{uu} d\Omega$, the elastic matrix $\mathbf{K}_{uu} = \int_{\Omega} \mathbf{B}_{uu}^T \bar{\mathbf{C}} \mathbf{B}_{uu} d\Omega$, the electromechanical coupling matrix $\mathbf{K}_{\varphi u} = \int_{\Omega} \mathbf{B}_{\varphi\varphi}^T \bar{\boldsymbol{\varepsilon}} \mathbf{B}_{uu} d\Omega$, the permittivity matrix $\mathbf{K}_{\varphi\varphi} = \int_{\Omega} \mathbf{B}_{\varphi\varphi}^T \bar{\boldsymbol{\kappa}} \mathbf{B}_{\varphi\varphi} d\Omega$, the mechanical load vector $\mathbf{F} = \int_{\Omega} \mathbf{N}_{uu}^T \mathbf{F}_V d\Omega + \int_{\Gamma} \mathbf{N}_{uu}^T \mathbf{F}_S d\Gamma$, and the charge vector $\mathbf{Q} = \int_{\Omega} \mathbf{N}_{\varphi\varphi}^T \bar{q} d\Omega + \int_{\Gamma} \mathbf{N}_{\varphi\varphi}^T \bar{Q} d\Gamma$.

2.4. Inclusion of FGPM shunted damping

The different shunt circuits connected to the piezoelectric electrodes induce a relation between the electric potential vector $\hat{\boldsymbol{\phi}}(t)$ and the electric charge vector $\mathbf{Q}(t)$ through the following general equation:

$$\mathfrak{R}(\mathbf{Q}(t)) + \mathfrak{J}(\hat{\boldsymbol{\phi}}(t)) = 0 \quad (8)$$

where \mathfrak{R} and \mathfrak{J} are linear differential operators with respect to time t . The closed circuit condition can be recovered for $\mathfrak{R} = \mathbf{0}$ and $\mathfrak{J} = \mathbf{I}$, and $\mathfrak{R} = \mathbf{I}$ and $\mathfrak{J} = \mathbf{0}$ give the open circuit one. The effects of shunted FGPM damping must be introduced in Eq. (7) and Eq. (7.b) is expressed in terms of the electric charge vector $\mathbf{Q}(t)$:

$$\hat{\boldsymbol{\phi}}(t) = \mathbf{K}_{\varphi\varphi}^{-1}(\mathbf{Q}(t) - \mathbf{K}_{\varphi u}\hat{\mathbf{u}}(t)) \quad (9)$$

Substituting Eq. (9) into Eqs. (7.a) and (8) leads to the following general coupled dynamic equations of the shunted piezoelectric damping structural system:

$$\begin{bmatrix} \bar{\mathbf{M}}_{uu} & \bar{\mathbf{M}}_{uQ} \\ \bar{\mathbf{M}}_{Qu} & \bar{\mathbf{M}}_{QQ} \end{bmatrix} \begin{bmatrix} \hat{\mathbf{u}}(t) \\ \hat{\mathbf{Q}}(t) \end{bmatrix} + \begin{bmatrix} \bar{\mathbf{C}}_{uu} & \bar{\mathbf{C}}_{uQ} \\ \bar{\mathbf{C}}_{Qu} & \bar{\mathbf{C}}_{QQ} \end{bmatrix} \begin{bmatrix} \hat{\mathbf{u}}(t) \\ \hat{\mathbf{Q}}(t) \end{bmatrix} + \begin{bmatrix} \bar{\mathbf{K}}_{uu} & \bar{\mathbf{K}}_{uQ} \\ \bar{\mathbf{K}}_{Qu} & \bar{\mathbf{K}}_{QQ} \end{bmatrix} \begin{bmatrix} \hat{\mathbf{u}}(t) \\ \hat{\mathbf{Q}}(t) \end{bmatrix} = \begin{bmatrix} \mathbf{F}(t) \\ \mathbf{0} \end{bmatrix} \quad (10)$$

In the following subsections, Eq. (10) is specialized to the case of four different shunt circuits considered in the present study.

2.4.1. R-L shunt circuit

When the classical R-L shunt circuits are considered, Eq. (8) reduces to:

$$\mathbf{L}\dot{\mathbf{Q}}(t) + \mathbf{R}\mathbf{Q}(t) + \hat{\boldsymbol{\phi}}(t) = \mathbf{0} \quad (11)$$

where \mathbf{L} and \mathbf{R} are inductance and resistance matrices, respectively. $\mathbf{I} = -\dot{\mathbf{Q}}$ denotes the electric current flowing in the shunt circuits. Substituting Eq. (9) into Eqs. (7.a) and (11), the following coupled dynamic system is obtained:

$$\begin{bmatrix} \mathbf{M}_{uu} & \mathbf{0} \\ \mathbf{0} & \mathbf{L} \end{bmatrix} \begin{bmatrix} \hat{\mathbf{u}}(t) \\ \dot{\mathbf{Q}}(t) \end{bmatrix} + \begin{bmatrix} \mathbf{0} & \mathbf{0} \\ \mathbf{0} & \mathbf{R} \end{bmatrix} \begin{bmatrix} \hat{\mathbf{u}}(t) \\ \mathbf{Q}(t) \end{bmatrix} + \begin{bmatrix} \mathbf{K}_{uu} - \mathbf{K}_{u\varphi}\mathbf{K}_{\varphi\varphi}^{-1}\mathbf{K}_{\varphi u} & \mathbf{K}_{u\varphi}\mathbf{K}_{\varphi\varphi}^{-1} \\ -\mathbf{K}_{\varphi\varphi}^{-1}\mathbf{K}_{\varphi u} & \mathbf{K}_{\varphi\varphi}^{-1} \end{bmatrix} \begin{bmatrix} \hat{\mathbf{u}}(t) \\ \mathbf{Q}(t) \end{bmatrix} = \begin{bmatrix} \mathbf{F}(t) \\ \mathbf{0} \end{bmatrix} \quad (12)$$

2.4.2. Resistive shunt

In this case, the following relation exists between $\hat{\boldsymbol{\phi}}$ and \mathbf{Q} :

$$\mathbf{R}\mathbf{Q}(t) + \hat{\boldsymbol{\phi}}(t) = \mathbf{0} \quad (13)$$

After substituting Eq. (9) into the above equation and Eq. (7.a), the following coupled system is obtained:

$$\begin{bmatrix} \mathbf{M}_{uu} & \mathbf{0} \\ \mathbf{0} & \mathbf{0} \end{bmatrix} \begin{bmatrix} \hat{\mathbf{u}}(t) \\ \dot{\mathbf{Q}}(t) \end{bmatrix} + \begin{bmatrix} \mathbf{0} & \mathbf{0} \\ \mathbf{0} & \mathbf{R} \end{bmatrix} \begin{bmatrix} \hat{\mathbf{u}}(t) \\ \mathbf{Q}(t) \end{bmatrix} + \begin{bmatrix} \mathbf{K}_{uu} - \mathbf{K}_{u\varphi}\mathbf{K}_{\varphi\varphi}^{-1}\mathbf{K}_{\varphi u} & \mathbf{K}_{u\varphi}\mathbf{K}_{\varphi\varphi}^{-1} \\ -\mathbf{K}_{\varphi\varphi}^{-1}\mathbf{K}_{\varphi u} & \mathbf{K}_{\varphi\varphi}^{-1} \end{bmatrix} \begin{bmatrix} \hat{\mathbf{u}}(t) \\ \mathbf{Q}(t) \end{bmatrix} = \begin{bmatrix} \mathbf{F}(t) \\ \mathbf{0} \end{bmatrix} \quad (14)$$

2.4.3. RIL shunt circuit

When a RIL shunt circuit is connected to the FGPM electrodes, the Eq. (8) is written as:

$$\mathbf{L}\dot{\mathbf{Q}}(t) + \mathbf{L}\mathbf{R}^{-1}\mathbf{Q}(t) + \hat{\boldsymbol{\phi}}(t) = \mathbf{0} \quad (15)$$

By substituting expression (9) for $\hat{\boldsymbol{\phi}}(t)$ in Eqs. (7.a) and (15), the following coupled system is then obtained:

$$\begin{bmatrix} \mathbf{M}_{uu} & \mathbf{0} \\ \mathbf{0} & \mathbf{L} \end{bmatrix} \begin{bmatrix} \hat{\mathbf{u}}(t) \\ \dot{\mathbf{Q}}(t) \end{bmatrix} + \begin{bmatrix} \mathbf{0} & \mathbf{0} \\ -\mathbf{L}\mathbf{R}^{-1}\mathbf{K}_{\varphi\varphi}^{-1}\mathbf{K}_{\varphi u} & \mathbf{L}\mathbf{R}^{-1}\mathbf{K}_{\varphi\varphi}^{-1} \end{bmatrix} \begin{bmatrix} \hat{\mathbf{u}}(t) \\ \mathbf{Q}(t) \end{bmatrix} + \begin{bmatrix} \mathbf{K}_{uu} - \mathbf{K}_{u\varphi}\mathbf{K}_{\varphi\varphi}^{-1}\mathbf{K}_{\varphi u} & \mathbf{K}_{u\varphi}\mathbf{K}_{\varphi\varphi}^{-1} \\ -\mathbf{K}_{\varphi\varphi}^{-1}\mathbf{K}_{\varphi u} & \mathbf{K}_{\varphi\varphi}^{-1} \end{bmatrix} \begin{bmatrix} \hat{\mathbf{u}}(t) \\ \mathbf{Q}(t) \end{bmatrix} = \begin{bmatrix} \mathbf{F}(t) \\ \mathbf{0} \end{bmatrix} \quad (16)$$

2.4.4. R-LIIC shunt circuit

In case of R-LIIC circuits, Eq. (8) becomes

$$\mathbf{L}\dot{\mathbf{Q}}(t) + \mathbf{R}\mathbf{Q}(t) + \mathbf{L}\mathbf{C}\hat{\boldsymbol{\phi}}(t) + \mathbf{R}\mathbf{C}\hat{\boldsymbol{\phi}}(t) + \hat{\boldsymbol{\phi}}(t) = \mathbf{0} \quad (17)$$

where \mathbf{C} is the admittance matrix. Adopting the approach employed in the previous subsections, the following coupled

equation is obtained for the considered dynamic system:

$$\begin{aligned} \begin{bmatrix} \mathbf{M}_{uu} & \mathbf{0} \\ -\mathbf{LCK}_{\varphi\varphi}^{-1}\mathbf{K}_{\varphi u} & \mathbf{L} + \mathbf{LCK}_{\varphi\varphi}^{-1} \end{bmatrix} \begin{bmatrix} \hat{\mathbf{u}}(t) \\ \hat{\mathbf{Q}}(t) \end{bmatrix} + \begin{bmatrix} \mathbf{0} & \mathbf{0} \\ -\mathbf{RCK}_{\varphi\varphi}^{-1}\mathbf{K}_{\varphi u} & \mathbf{R} + \mathbf{RCK}_{\varphi\varphi}^{-1} \end{bmatrix} \begin{bmatrix} \hat{\mathbf{u}}(t) \\ \hat{\mathbf{Q}}(t) \end{bmatrix} \\ + \begin{bmatrix} \mathbf{K}_{uu} - \mathbf{K}_{u\varphi}\mathbf{K}_{\varphi\varphi}^{-1}\mathbf{K}_{\varphi u} & \mathbf{K}_{u\varphi}\mathbf{K}_{\varphi\varphi}^{-1} \\ -\mathbf{K}_{\varphi\varphi}^{-1}\mathbf{K}_{\varphi u} & \mathbf{K}_{\varphi\varphi}^{-1} \end{bmatrix} \begin{bmatrix} \hat{\mathbf{u}}(t) \\ \hat{\mathbf{Q}}(t) \end{bmatrix} = \begin{bmatrix} \mathbf{F}(t) \\ \mathbf{0} \end{bmatrix} \end{aligned} \quad (18)$$

2.5. State-space design

In this section, the state-space approach is employed for solving the coupled dynamic equations of the shunted piezoelectric damping structural system (Eq. (10)). The state-space approach is the basis of the modern control and is efficient to analyze systems with several inputs and outputs. In this approach, dynamic systems are described by means of first order differential equations [25]. Introducing the state-space variable $\mathbf{x}(t)$ as $\mathbf{x}(t) = \{\boldsymbol{\eta}(t), \dot{\boldsymbol{\eta}}(t)\}^T$, Eq. (10) can be written in the following state-space form:

$$\dot{\mathbf{x}}(t) = \mathbf{A} \mathbf{x}(t) + \mathbf{B} \mathbf{f}(t) \quad (19)$$

where

$$\mathbf{A} = \begin{bmatrix} \mathbf{0} & \mathbf{I} \\ -\bar{\mathbf{M}}^{-1}\bar{\mathbf{K}} & -\bar{\mathbf{M}}^{-1}\bar{\mathbf{C}} \end{bmatrix}, \quad \mathbf{B} = \begin{bmatrix} \mathbf{0} \\ \bar{\mathbf{M}}^{-1} \end{bmatrix}, \quad \boldsymbol{\eta}(t) = \begin{bmatrix} \hat{\mathbf{u}}(t) \\ \hat{\mathbf{Q}}(t) \end{bmatrix}, \quad \mathbf{f}(t) = \begin{bmatrix} \mathbf{F}(t) \\ \mathbf{0} \end{bmatrix}$$

$$\bar{\mathbf{M}} = \begin{bmatrix} \bar{\mathbf{M}}_{uu} & \bar{\mathbf{M}}_{uQ} \\ \bar{\mathbf{M}}_{Qu} & \bar{\mathbf{M}}_{QQ} \end{bmatrix}, \quad \bar{\mathbf{C}} = \begin{bmatrix} \bar{\mathbf{C}}_{uu} & \bar{\mathbf{C}}_{uQ} \\ \bar{\mathbf{C}}_{Qu} & \bar{\mathbf{C}}_{QQ} \end{bmatrix}, \quad \bar{\mathbf{K}} = \begin{bmatrix} \bar{\mathbf{K}}_{uu} & \bar{\mathbf{K}}_{uQ} \\ \bar{\mathbf{K}}_{Qu} & \bar{\mathbf{K}}_{QQ} \end{bmatrix}$$

and \mathbf{I} denotes the identity matrix. \mathbf{A} and \mathbf{B} are called the state-space and dynamic input matrices, respectively. The general solution to Eq. (19) is:

$$\mathbf{x}(t) = e^{\mathbf{A}t} \mathbf{x}(0) + \int_0^t e^{\mathbf{A}(t-\tau)} \mathbf{B} \mathbf{f}(\tau) d\tau \quad (20)$$

3. Case studies and discussion

This section aims at evaluating the performance of the proposed FGPM shunt damping approach and its associated finite element implementation for passive vibration control of laminated composite beams. First, the performance of the proposed finite element formulation is evaluated through comparison with other results available in the literature. Then, the forced and free vibrations of some laminated composite beams are controlled using the proposed FGPM shunt damping technique. Comparisons have been made between the damping performances of the different shunt circuits.

3.1. Example 1

A four-layered $[0^\circ/90^\circ/90^\circ/0^\circ]$ cantilever beam with two FGPM patches perfectly bonded on its top and bottom surfaces is considered (see Fig. 3). The beam is made of graphite epoxy (GE) layers with the mechanical properties given in Table 1. The thickness of GE layers and FGPM patches are $h_{GE}=0.5$ mm and $h_p=0.125$ mm, respectively. The beam and FGPM patch lengths are $L=0.25$ m and $L_p=0.125$ m, and their common width is $b=1$ m. The FGPM patches are installed on the beam and have opposite poling directions. The piezoelectric patches are made of PZT-5J based exponentially graded piezoelectric layers with the following material properties:

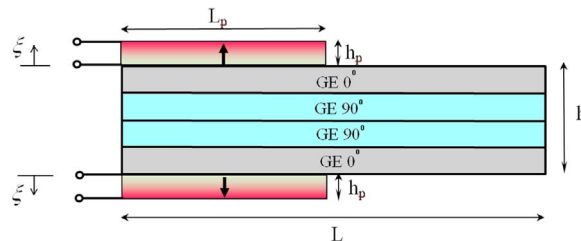


Fig. 3. Configuration of the considered smart laminated composite beam (the arrows drawn inside the FGPM layers represent the poling direction).

Table 1
Mechanical and electrical properties of materials.

	PZT-5J [12]	GE [12]	PZT-5A [26]
c_{11}^0 (GPa)	82.29	183.44	99.20
c_{12}^0 (GPa)	34.08	4.36	54.02
c_{22}^0 (GPa)	82.29	11.66	99.20
c_{13}^0 (GPa)	30.24	4.36	50.78
c_{23}^0 (GPa)	30.24	3.92	50.78
c_{33}^0 (GPa)	59.77	11.66	86.86
c_{44}^0 (GPa)	21.27	2.87	21.10
c_{55}^0 (GPa)	21.27	7.17	21.10
c_{66}^0 (GPa)	24.10	7.17	22.60
e_{15}^0 (C m ⁻²)	14.25	0	12.33
e_{24}^0 (C m ⁻²)	14.25	0	12.33
e_{31}^0 (C m ⁻²)	-10.49	0	-7.21
e_{32}^0 (C m ⁻²)	-10.49	0	-7.21
e_{33}^0 (C m ⁻²)	16.58	0	15.12
χ_{11}^0 (10 ⁻⁹ F m ⁻¹)	14.53	1.53	1.53
χ_{22}^0 (10 ⁻⁹ F m ⁻¹)	14.53	1.53	1.53
χ_{33}^0 (10 ⁻⁹ F m ⁻¹)	10.12	1.53	1.50
ρ (kg/m ³)	7400	1590	7800

$$c_{kl} = c_{kl}^0 e^{a\xi/h_p}, \quad e_{ik} = e_{ik}^0 e^{a\xi/h_p}, \quad \chi_{ij} = \chi_{ij}^0 e^{a\xi/h_p}, \quad \rho = \rho^0 e^{a\xi/h_p} \quad (21)$$

where a is a constant characterizing the degree of the material gradient along the thickness direction. c_{kl}^0 , e_{ik}^0 , χ_{ij}^0 and ρ^0 are the values of material properties at the bottom and top of the upper and lower FGPM patches, respectively. ξ in Eq. (21) is a local coordinate defined within FGPM layers and should be measured from its reference (lower or upper) surface (see Fig. 3). For the gradient factors, five different values $a = -2, -1, 0, 1$ and 2 are considered. The variations of the material properties in the top and bottom FGPM layers are symmetric as shown in Fig. 3.

3.1.1. Static tests

First, the static electro-mechanical response of the smart beam is evaluated. To this aim, three different configurations are considered: the sensor configuration, the actuator configuration and the sensor-actuator configuration. In sensor configuration, a mechanical force of $F=1$ N is applied at the free end of the smart beam. The electric boundary conditions of the two FGPM patches are assumed to be short circuit (SC). In the actuator configuration, the lower electrodes of both FGPM patches are grounded while a voltage $V=1$ V is applied through the top electrode terminal. Concerning the sensor-actuator configuration, both shearing force $F=1$ N and applied voltage $V=1$ V are considered acting together. The mesh convergence study shows that a mesh with 10 elements of equal lengths is adequate to model the considered beam under different configurations (see Table 2). Based on the mesh convergence study, a mesh with 10 finite elements (87 DOFs) is used for solving the present and all subsequent problems. The tip deflection of the smart beam is calculated using the present finite element model for five material gradient composition $a = -2, -1, 0, 1$ and 2 . The results are shown in Table 3. For $a=0$, the considered smart composite beam of the present example reduces to the smart beam examined by Alaimo et al. [12]. They analyzed this problem using a 1D beam element based on the first-order shear deformation theory. In Table 3, the present results are compared with both the results of Alaimo et al. and the results obtained from 2D finite element analysis. The comparison of the computational cost is also given in this table. The excellent matching results demonstrate the efficiency of the present refined sinus finite element model.

Table 2
Tip deflection of the cantilever smart laminated beam for different number of elements: $a=-2$.

Configuration	Number of elements			
	4	10	20	40
Sensor [10 ⁻⁶ m]	46.2335	46.2342	46.2345	46.2346
Actuator [10 ⁻⁶ m]	-2.5257	-2.5257	-2.5256	-2.5255
Sensor-actuator [10 ⁻⁶ m]	43.7078	43.7085	43.7089	43.7091
Number of DOFs	39	87	167	327

Table 3Tip deflection ($w_{tip,static}$) of the cantilever smart laminated beam under different configurations.

Configuration	a = -2	a = -1	a = 0			a = 1	a = 2
	present	present	present	Alaimo et al. [12]	2D finite element [12]	present	present
Sensor [$10^{-6}m$]	46.2342	45.0211	42.9412	42.9370	42.9470	39.4213	33.9058
Actuator [$10^{-6}m$]	-2.5257	-3.6129	-5.4622	-5.4607	-5.4495	-8.5689	-13.4033
Sensor-actuator [$10^{-6}m$]	43.7085	41.4082	37.479	37.4763	37.4975	30.8524	20.5025
Number of DOFs	87	87	87	96	81153	87	87

3.1.2. Free vibration tests

The lowest six natural frequencies of the beam with open circuit (OC) and SC electric boundary conditions are predicted using the present finite element model. The results for different values of material gradient indexes are summarized in Tables 4 and 5. In Table 4, the SC natural frequencies of the beam obtained from the present finite element formulation have been compared with the results of Alaimo et al. and the results obtained from 2D finite element analysis. It is seen again that the results obtained using the present formulation are in good agreement with those reported using the 1D and 2D finite element models.

The SC and OC natural frequencies listed in Tables 4 and 5 were used to evaluate the EEMCCs of the considered smart beam. The numerical values of EEMCCs corresponding to the first six vibrating modes of the beam are shown in Table 6. The EEMCC for structure with piezoelectric elements, vibrating in the j -th mode, is defined as [7]:

$$k_j^{eff} = \sqrt{\frac{(\omega_j^{OC})^2 - (\omega_j^{SC})^2}{(\omega_j^{SC})^2}} \quad (22)$$

where ω_j^{SC} and ω_j^{OC} denote the j -th natural frequencies of the electromechanical system in short and open circuit conditions, respectively. It is worthy to note that the EEMCC is an important parameter affecting the performance of passive shunt damping systems [27]. It can be observed from Table 6 that all EEMCCs of the cantilever smart composite beam correspondent to different vibrating modes increase with the increasing of the material gradient index of the FGPM patches. It is also seen from Table 6 that value of the EEMCC for the first bending mode of the beam is higher than other ones regardless of the values of the material gradient index. Since the FGPM patches are bonded near the clamped end where the strains are higher for the first bending mode, such behavior is expected. The low values of EEMCC for other bending modes may be due to the occurrence of the *charge cancellation* phenomenon [28].

3.2. Example 2

Once the accuracy of the proposed finite element has been demonstrated for static and free vibration analyses, its damping behavior for different shunted circuits is investigated in this section. The FGPM laminated beam is the same as in the previous example. The two FGPM patches are connected to distinct shunt circuits characterized by the same electrical components. R shunt, R-L shunt, R-LIIC shunt and RIIL shunt circuits are considered in this example. A mechanical step time force of $F(t)=1N$ is applied at the free end of the beam. This step time force is shown in Fig. 4.

In order to validate the performance of the proposed refined sinus finite element formulation for passive vibration damping of composite beams, a comparison has been made with the other results available in the literature. A R-L shunt circuit with $R=34\Omega$ and $L=0.4832H$ is connected to both FGPM patches. The values of material gradient composition is assumed to be $a=0$. The time history response of the normalized tip deflection ($w_{tip}(t)/w_{tip,static}$) of the beam under step loading is shown and compared with the results of Alaimo et al. [12] in Fig. 5. It is seen that there is an excellent agreement between the present results and those obtained by Alaimo et al. based on FSDT.

Table 4

SC natural frequencies of the smart laminated beam.

	a = -2	a = -1	a = 0			a = 1	a = 2
	present	present	present	Alaimo et al. [12]	2D FE [12]	present	present
ω_1^{SC}	53.074	53.695	54.816	54.827	54.81	56.893	60.698
ω_2^{SC}	312.52	308.37	301.69	302.27	301.5	291.22	276.38
ω_3^{SC}	864.51	852.35	834.26	837.83	833.5	809.27	779.31
ω_4^{SC}	1676.01	1648.68	1605.39	1617.8	1602	1540.04	1453.15
ω_5^{SC}	2748.01	2708.89	2649.45	2680.6	2642	2563.24	2447.29
ω_6^{SC}	4041.14	3974.94	3870.80	3935.7	3855	3716.42	3519.83

Table 5
OC natural frequencies of the smart laminated beam.

	a = -2	a = -1	a = 0	a = 1	a = 2
ω_1^{OC}	53.331	54.069	55.394	57.830	62.237
ω_2^{OC}	312.52	308.39	301.70	291.25	276.43
ω_3^{OC}	864.82	852.81	834.96	810.39	781.16
ω_4^{OC}	1676.01	1648.69	1605.41	1540.09	1453.28
ω_5^{OC}	2748.31	2709.33	2650.10	2564.23	2448.79
ω_6^{OC}	4041.15	3974.96	3870.87	3716.59	3520.35

Table 6
EEMCCs for the smart FGMP laminated beam.

	a				
	-2	-1	0	1	2
k_1^{eff}	0.0985	0.1182	0.1456	0.1822	0.2266
k_2^{eff}	0.0068	0.0084	0.0106	0.0138	0.0174
k_3^{eff}	0.0271	0.0328	0.0410	0.0527	0.0690
k_4^{eff}	0.0015	0.0027	0.0043	0.0076	0.0130
k_5^{eff}	0.0148	0.0178	0.0221	0.0278	0.0350
k_6^{eff}	0.0021	0.0033	0.0056	0.0098	0.0172

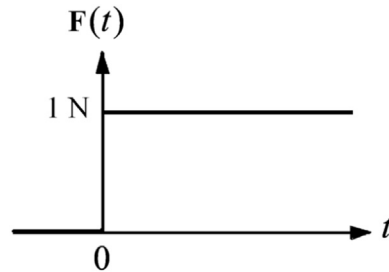


Fig. 4. The history of the applied step time force.

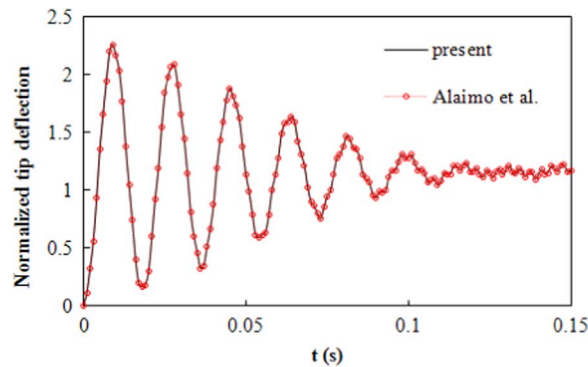


Fig. 5. Tip deflection of the cantilever laminated beam with R-L shunt circuit ($R=34\Omega$).

3.2.1. R shunt circuit

The electrodes of two FGPM patches are connected to the pure resistive circuits. In order to find an optimal value for resistor R , the minimum value of a proposed damping performance index is seek. The proposed damping performance index is defined below:

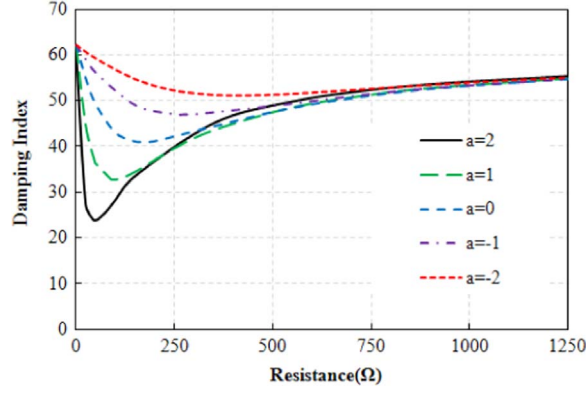


Fig. 6. Variations of damping performance index with respect to resistor values (R shunt).

$$y = 200 \int_0^t \left| \frac{w_{tip}(t) - w_{tip,static}}{w_{tip,static}} \right| dt \quad (23)$$

It is worthy to note that the above introduced damping performance index is indeed relevant to the area under the tip deflection-time graph. In Ref. [12], a similar damping performance index is employed. Variations of the damping performance index with respect to the resistance of shunt circuit are shown in Fig. 6. For the material gradient index, five values $a = -2, -1, 0, 1$ and 2 is considered. The time history of the normalized tip deflection of the laminated beam is shown in Fig. 7 for the optimal resistor values. It is seen from these figures that the damping performance of the resistive shunt circuits increases with the increasing of the material gradient composition. The depicted graphs of Fig. 6 also reveal that the optimum value of the resistors reduces with the increasing of the material gradient composition of FGPM patches. For $a = -2$, the minimum value of y is 2.14 larger than that of $a = 2$. The optimal value of resistor R is also 8.43 times larger than that of $a = 2$. The EEMCCs of the smart beam increase with the increasing of the material gradient composition of the FGPM patches, leading to the improvement of the shunt damping performance of the system.

3.2.2. R-L shunt circuit

The R-L shunt configuration is considered here. In contrast to R-shunt circuit which acts on the structure vibration despite of its frequency content, the shunt circuits containing inductor can only minimize the structure vibration state associated to a particular natural frequency of the structure. This is achieved by tuning the natural frequency of the electrical circuits to that of the structure to be damped out [8]:

$$L = \frac{1}{(2\pi\omega_j)^2 C_p} \quad (24)$$

where C_p is the piezoelectric transducer capacitance and ω_j denotes the j th natural frequency (Hz) of the structure to be damped out. Similar to the resistive shunt circuit, the optimal value of resistor R is determined by minimizing the value of the proposed damping performance index y . The influence of the resistance on the damping performance index is shown in Fig. 8 for the five values of the material gradient index $a = -2, -1, 0, 1$ and 2 . The transient responses in terms of beam tip deflection are reported in Fig. 9 for the optimal resistor values. Similar to the resistive shunt circuit case, it is seen again that the minimum value of the damping performance index increases with the increasing of the material gradient composition.

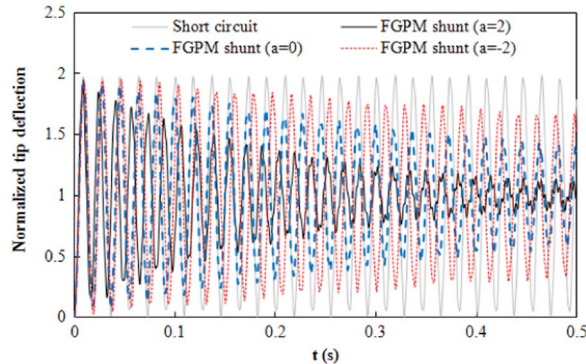


Fig. 7. Time history of normalized tip deflection of the beam with R shunt circuits for optimal value of resistors.

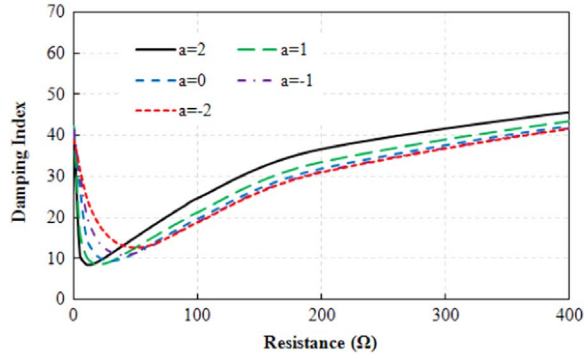


Fig. 8. Variations of damping performance index with respect to resistor values (R-L shunt).

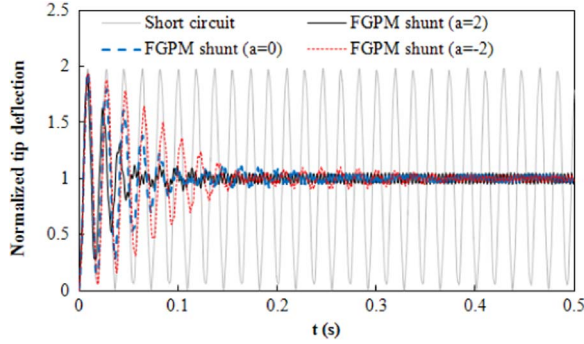


Fig. 9. Time history of normalized tip deflection of the beam with R-L shunt circuits for optimal values of resistors.

The optimum values of the resistor reduce also with the increasing of material gradient composition of FGPM patches. For $a=2$, the optimum value of the resistor and the minimum value of the damping performance index are 13Ω and 8.47 m.s , respectively. In case of $a=-2$, these values are 50Ω and 12.66 ms .

3.2.3. RIL shunt circuit

The classical RIL shunt circuits, tuned to the first beam mode are connected to the FGPM patches. The optimal value of the resistor R is determined by minimizing the value of the proposed damping performance index. For different material gradient index, variations of shunt resistance with respect to the damping performance index are depicted in Fig. 10. The time history of the normalized tip deflection of smart beam is reported in Fig. 11 for the optimal resistor values. The obtained numerical results of this example reveal again this fact that with increasing the material gradient composition, one can increase the performance of shunt damping without stress concentrations near the interfaces between the beam and piezoelectric patches.

3.2.4. R-LIC shunt circuit

The R-LIC shunt circuits, tuned to the first beam mode are connected to the electrodes of two FGPM patches. In order to

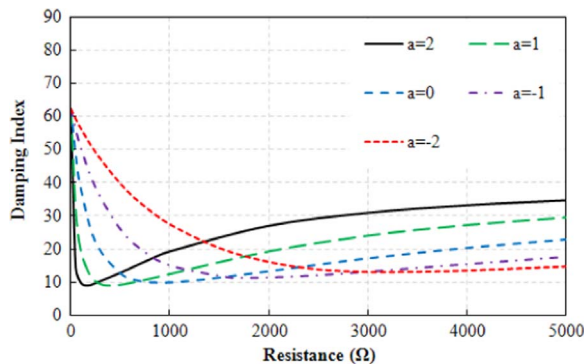


Fig. 10. Variations of damping performance index with respect to resistor values (RIL shunt).

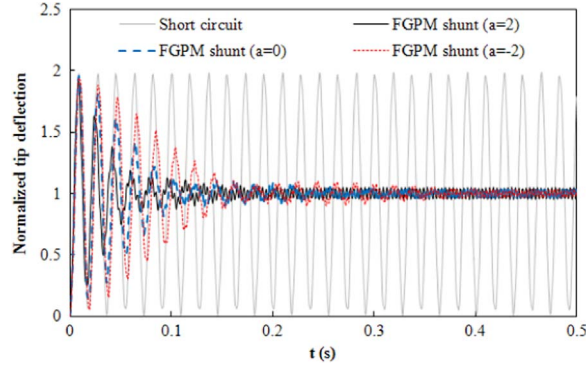


Fig. 11. Time history of normalized tip deflection of the beam with RIL shunt circuits for optimal values of resistors.

achieve the maximum damping performance, the value of the inductance is adopted as follow [8]:

$$L = \frac{1}{(2\pi\omega_1)^2(C_p + C)} \quad (25)$$

First, the value of the external capacity C in the R-LIIC shunt circuits is chosen equal to the capacity of the FGPM patches with $a=0$. In other words, it is assumed that $C=C_p=17.1 \mu\text{F}$. Variations of damping performance index with respect to the resistor values are depicted in Fig. 12 for five values of the material gradient composition $a = -2, -1, 0, 1$ and 2 . In Fig. 13, the time history of the normalized tip deflection of the laminated beam is depicted for the optimal resistor values. Due to the increasing of the EEMCCs, it is seen again that the damping performance of the R-LIIC shunt circuit increases with the increasing of the material gradient composition. With the increasing of material gradient composition from $a = -2$ to $a=2$, the minimum value of the damping performance index decreases from 21.53 ms to 9.02 ms. In contrast to other shunt circuit configurations, the optimum values of the resistor in R-LIIC shunt circuits are not sensitive to the change in the material gradient composition of the FGPM patches (see Fig. 12).

The effects of the external capacity on the damping performance of FGPM shunt circuits are investigated in Fig. 14 with $a=2$ for the material gradient composition. For further comparisons, the obtained numerical results are also shown in Table 7. It can be observed that with the increasing of the value of the external capacity C , the damping performance of the shunt circuits reduces slightly. However, R-LIIC parallel circuit leads to the reduction in the tuning value of the inductance L due to the insertion of an external capacity C in parallel to the R-L branch. Moreover, the optimal value of the resistor R reduces slightly with the increasing of the external capacity C . It can be concluded from these numerical results that the value of the external capacitance C cannot be chosen too large in order to have an effective damping system. In other words, there are limitations on the reduction of the tuning inductance L and the optimum resistance R achievable with an R-LIIC shunt circuit in practical conditions.

3.2.5. Comparison between different shunt circuits

In order to have a comparison between the damping performance of different shunt circuits connected to electrodes of the FGPM patches, the obtained numerical results of the previous subsections are summarized in Table 8. It is seen from this table that the R-L shunt circuit is more effective in passive damping of vibrations than the other shunt circuits regardless of the values of the material gradient composition. The numerical results of Table 8 show also that the pure resistive shunt circuit is less effective in the attenuation of vibrations in comparison to other shunt circuits. However, R-shunt circuit has this particular advantage which can attenuate the vibration of a structure despite of its frequency content. Although the

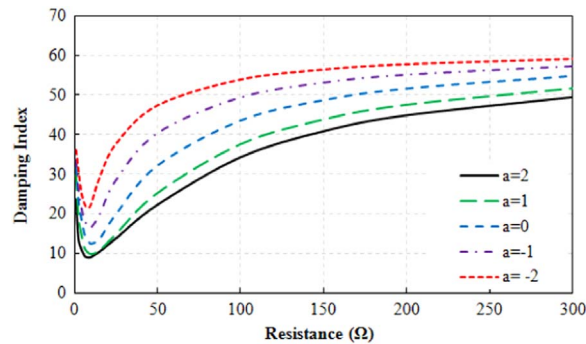


Fig. 12. Variations of damping performance index with respect to resistor values (R-LIIC shunt).

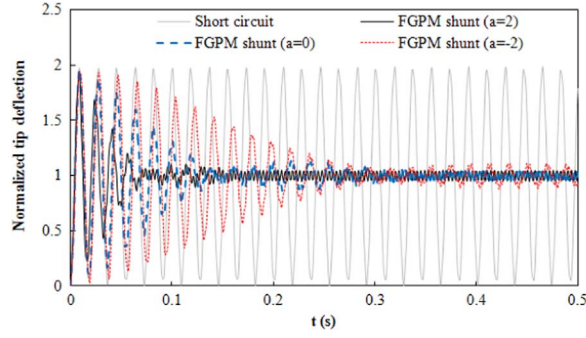


Fig. 13. Time history of normalized tip deflection of the beam with R-LIIC shunt circuits for optimal values of resistors.

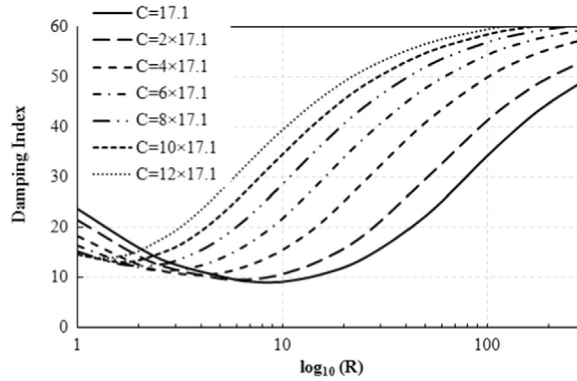


Fig. 14. Effect of the external capacitor on the performance of the FGPM shunted damping ($a=2$).

Table 7

Comparison between damping performance of R-LIIC shunt circuits with different values of external capacity ($a=2$).

C (μF)	L (H)	θ_{\min} (ms)	R_{opt} (Ω)
0	0.1198	8.50	13
17.1	0.0912	9.02	9
2×17.1	0.0737	9.54	6
4×17.1	0.0532	10.50	4
6×17.1	0.0416	11.48	3
8×17.1	0.0342	12.29	2
10×17.1	0.0290	13.12	1.7
12×17.1	0.0252	13.90	1.3

Table 8

Comparison between the damping performance of different shunt circuits.

a	R circuit			R-L circuit			RIIL circuit			R-LIIC ($C=C_p$)		
	y_{\min}	R_{opt}	L_{opt}	y_{\min}	R_{opt}	L_{opt}	y_{\min}	R_{opt}	L_{opt}	y_{\min}	R_{opt}	L_{opt}
2	23.85	49	-	8.47	13	0.1198	9.01	160	0.1198	9.02	9	0.0912
1	32.73	96	-	8.45	20	0.2580	8.99	390	0.2580	10.03	9	0.1630
0	40.93	171	-	9.35	30	0.4832	9.90	910	0.4832	12.47	10	0.2415
-1	46.95	280	-	10.87	40	0.8024	11.36	1800	0.8024	16.51	10	0.3108
-2	51.12	413	-	12.66	50	1.2058	13.09	3200	1.2058	21.53	8	0.3637

damping performance of the R-L and RIIL shunt circuits are almost similar together, the optimum values of resistor in a RIIL shunt circuit is much higher than R-L shunt one. When R-L shunt circuits are connected to the FGPM patches with material gradient composition $a=-2$, the optimum values of R is 50Ω . In case of RIIL shunt circuits, this value is 3200Ω . If both of the damping performance index and the limitations of electrical shunt components (inductance L and the resistance R) are considered simultaneously as damping criteria, it seems that the R-LIIC shunt circuit is a suitable choice for the practical conditions. With connecting the electrodes of the FGPM patches with $a=2$ to the R-LIIC shunt circuits instead of an R-L one,

the minimum values of the damping performance index does not change significantly. However, the optimum value of the resistor reduces more than 17 times. The reduction in the optimum values of the inductor is 1.3 times.

The obtained numerical results of Table 8 reveal that the values of inductance L reduce with the increasing of the material gradient composition whatever the type of shunt circuits. Since the natural frequencies of the smart laminated beam increase with the increasing of the material gradient composition of FGPM patches, the reduction in the inductance of shunt circuit is expected. Table 8 also shows that in all shunt circuit cases, the optimum value of the resistor R increase with the decreasing of the material gradient composition except in R-LIC shunt case.

3.3. Example 3

As a final example, the shunt passive vibration control of laminated composite beams by using the piezoelectric patches whose material properties vary along the thickness direction according to the power law distribution is studied. Geometry, material properties and the boundary conditions of the considered laminated composite beam are the same as those of the previous example. The only differences are the length and the material properties of the bonded top and bottom FGPM patches. In this section, the length of the FGPM patches are assumed to be $L_p=0.025$ m. The following distribution of material properties is considered along the thickness direction of the FGPM patches:

$$\psi = (1 - (\bar{z} + 0.5)^n)\psi^B + (\bar{z} + 0.5)^n\psi^T \quad (26)$$

where $\bar{z} = \frac{2}{z_{k+1}-z_k}x_3 - \frac{z_{k+1}+z_k}{z_{k+1}-z_k}$ and ψ is an arbitrary material property of the FGPM patch. ψ^T and ψ^B represent the values of ψ on the upper and lower surfaces of FGPM patches, respectively. The symbol n is the material gradient composition. In this example, the value of the n is assumed to be 5. In the FGPM patch bonded on the top of the laminated beam, the material properties vary from 100% PZT-5J at the lower surface to 100% PZT-5A at the upper surface. The elastic, piezoelectric and dielectric constants for these two piezoelectric materials can be found in Table 1. The variations of material properties in the FGPM patches bonded on the bottom surface of the cantilever beam are assumed to be in symmetrical configuration with that bonded on upper surface. The beam is subjected to an initial static deformed position, created by a mechanical shearing force $F=1$ N applied at the free end of the laminated beam. The lowest six natural frequencies of the laminated beam with OC and SC electric boundary conditions are shown in Table 9. In this table, the values of EEMCC corresponding to these six vibrating modes are also shown. It can be observed from this table that the values of the EEMCCs corresponding to the different vibrating modes of the smart beam are relatively high. Therefore, it is expected that all oscillations related to the lowest six vibrating modes of the laminated beam can be controlled effectively by using the appropriate shunt circuits.

Time history of the tip deflection of the beam with the classical R-L shunt circuits tuned to the first bending mode is shown in Fig. 15 for the optimal value of resistor ($R_{opt}=90 \Omega$). It is worthy to note that the optimal value of R has been calculated via the minimization of the following damping performance index:

$$y = \int_0^t |w_{tip}(t)| dt \quad (27)$$

Since the applied initial static deformed position is very close to the first bending mode shape of the laminated beam, it is clearly visible on Fig. 15 that the employed shunt circuits have a large damping effect on the oscillations. The difference of electric potential at the R-L shunt circuits connected to FGPM patches versus time is also shown in Fig. 16.

The driving-point receptance frequency response function (FRF) at the free end of the laminated beam (i.e. the response at the tip for an excitation at the same point) is presented in Fig. 17. In this figure, the tip laminated composite beam FRF is depicted under the following five electromechanical conditions:

- OC: the shunt is open circuit;
- R-L-1: the classical R-L shunt circuits tuned to the first beam mode (1F) are connected to the electrodes of the FGPM patches;
- R-L-2: the classical R-L shunt circuits tuned to the second beam mode (2F) are connected to the electrodes of the FGPM patches;
- R-L-3: the classical R-L shunt circuits tuned to the third beam mode (3F) are connected to the electrodes of the FGPM

Table 9
Natural frequencies and EEMCCs for the smart FGPM laminated beam ($n=5$).

Mode	ω^{OC} (rad/s)	ω^{SC} (rad/s)	k_{eff}
1	334.6316	333.4984	0.0825
2	2072.265	2067.170	0.0703
3	5729.989	5720.374	0.0580
4	11062.71	11051.79	0.0445
5	17984.76	17976.51	0.0303
6	26396.33	26392.88	0.0162

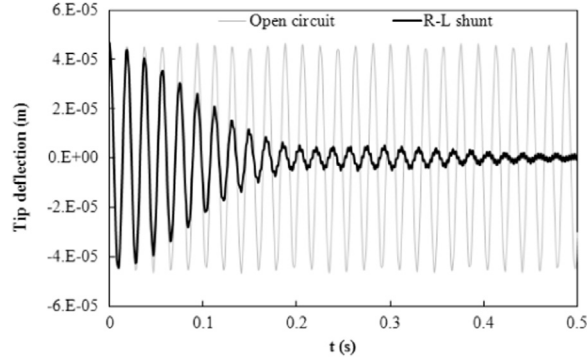


Fig. 15. Time history of tip deflection of the beam with R-L shunt circuits for the optimal values of resistors ($R_{opt}=90\Omega$).

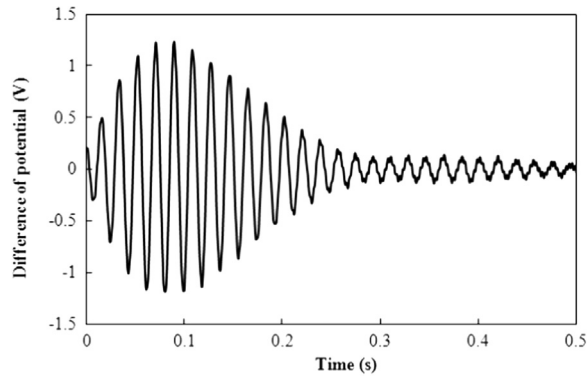


Fig. 16. Time history of the difference of electric potential at the R-L shunt circuits ($R_{opt}=90\Omega$).

patches;

- R-L-4: the classical R-L shunt circuits tuned to the fourth beam mode (4F) are connected to the electrodes of the FGPM patches;

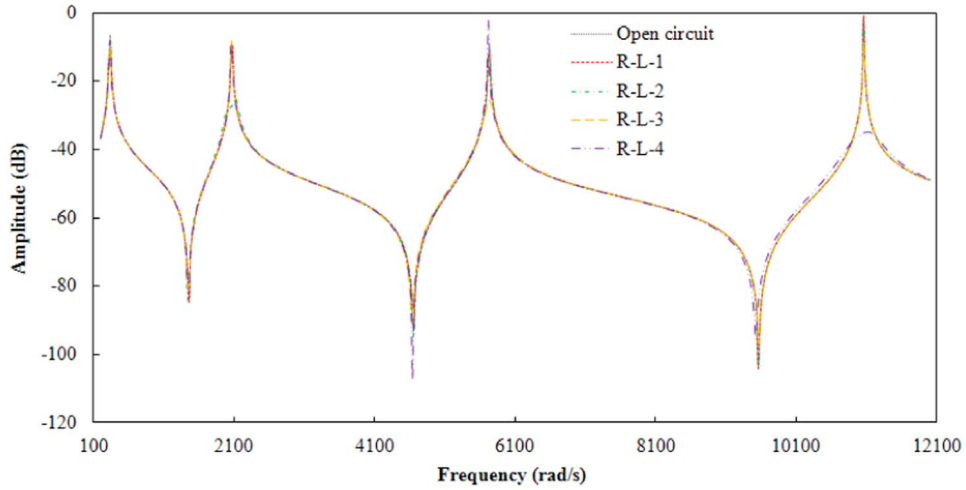
The optimal electrical parameters used in each shunt circuit are presented in Table 10. In this table, the optimal value of the resistor R is determined from the depicted graphs of Fig. 18. In these graphs, the reduction in the first four peak resonance frequency of the laminated beam is depicted versus the resistance of each considered shunt circuit. It can be concluded from Table 10 that the shunt circuits with lower values of electrical components are needed for the attenuation of higher vibrating modes of the laminated beam.

The depicted FRF graphs of the laminated beam (Fig. 17) show that the vibration reduction achieved by the FGPM shunts is excellent. The R-L shunt circuits reduce the first resonance peak about 5.74 dB, whereas its effect in the reduction of resonant peak correspond the other modes is negligible. The R-L shunt tuned on the second beam mode significantly reduces the 2F response (15.17 dB). Similar to the R-L-1 shunt circuits, the effect of R-L-2 shunt circuits in the reduction of resonant peak correspond the other modes are insignificant. The R-L-3 and R-L-4 shunt circuits reduce the 3F and 4F resonance peaks about 13.51 dB and 34.04 dB, respectively. The focus on the depicted graphs of Fig. 17 shows that the R-L-2 and R-L-4 shunt circuits have more broadband effects than the R-L-1 and R-L-3 shunt circuits.

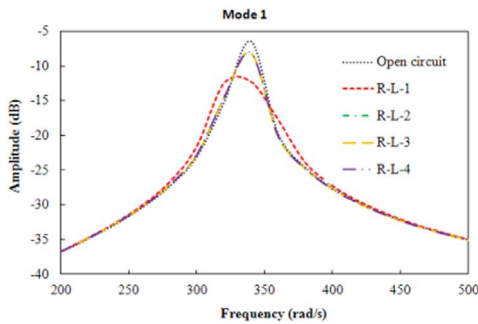
4. Conclusion

For the first time, the application of FGPMs for shunted passive vibration damping of laminated composite beams was investigated. A three-nodded beam element which is based on the refined sinus model kinematic was used in deriving the dynamic equations of the coupled system. The computational cost of the employed element is very low in comparison with the available layer-wise beam theories. Moreover, the continuity conditions between layers for displacements, transverse shear stress and the free conditions at the top and bottom surfaces of the beam are satisfied by the present kinematic. The main practical conclusions of the present paper may be summarized as follows:

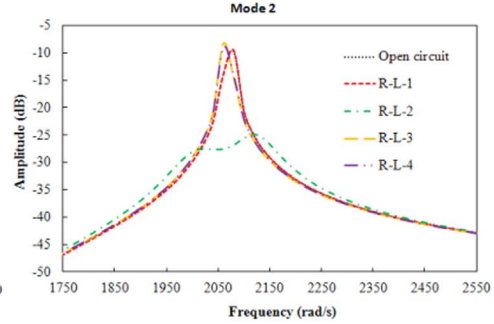
- Regardless of the values of the material gradient composition of FGPM, the R-L shunt circuit has the best performance in damping of vibrations.



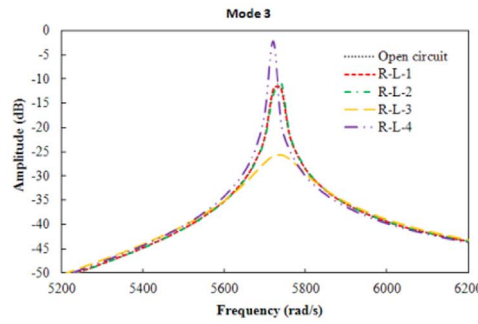
(a)



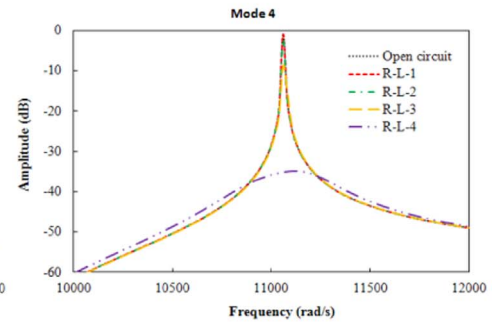
(b)



(c)



(d)



(e)

Fig. 17. Frequency response function of the laminated composite beam at its free end: (a) General view showing the first four beam resonances, (b) Detail of mode 1F resonance, (c) Detail of mode 2F resonance, (d) Detail of mode 3F resonance, (e) Detail of mode 4F resonance.

Table 10

The optimal electrical parameters used in FGPM shunt circuits.

	L_{opt} (H)	R_{opt} (Ω)
R-L-1	2.5494	63
R-L-2	0.0665	12
R-L-3	0.0087	10
R-L-4	0.0023	2

- Pure resistive shunt circuit is less effective in the attenuation of vibrations in comparison to other shunt circuits. However, R-shunt circuit can attenuate the vibration of a structure despite of its frequency content.
- For the same values of the damping performance index, the required resistance of an RIIL shunt circuit is much higher

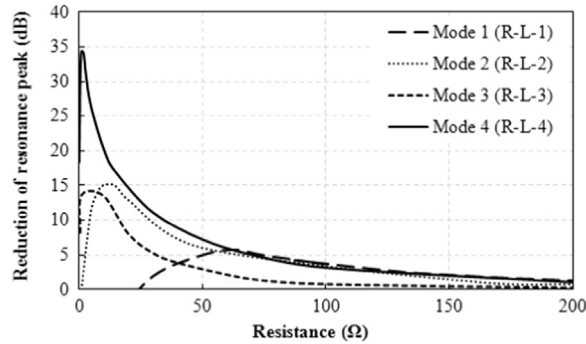


Fig. 18. The reduction in the peak resonance frequency with respect to the resistor values.

than R-L shunt one.

- Due to the insertion of an external capacity C in parallel to the R-L branch, R-LIIC shunt circuit leads to the reduction in the tuning value of the inductance L . For shunted damping of vibrations in practical conditions, R-LIIC shunt circuit seems to be the best suitable choice.
- The damping performance of different shunt circuits increases drastically with the increasing of the material gradient composition of FGPM transducers.
- The value of inductance L in all types of shunt circuits reduces with the increasing of the material gradient composition of FGPM.
- Expect the R-LIIC shunt circuit, the optimum value of the resistor R increase with the decreasing of the material gradient composition of FGPM.

Finally, the application of FGPM transducers for shunted damping increases the reliability of the passive control networks by decreasing the interface stress levels and consequently the decreasing of failure from the interfacial debonding.

Funding

The authors received no financial support for the research, authorship, and/or publication of this article.

Conflict of Interest

The authors declare that they have no conflict of interest.

References

- [1] S.B. Beheshti-Aval, M. Lezgy-Nazargah, Assessment of velocity-acceleration feedback in optimal control of smart piezoelectric beams, *Smart Struct. Syst.* 6 (8) (2010) 921–938.
- [2] C.R. Fuller, S.J. Elliot, P.A. Nelson, *Active Control of Vibration*, Academic Press, London, 1996.
- [3] G.A. Lesieutre, Vibration damping and control using shunted piezoelectric materials, *Shock Vib. Dig.* 30 (1998) 181–190.
- [4] N.W. Hagood, A. Von Flotow, Damping of structural vibrations with piezoelectric materials and passive electrical networks, *J. Sound Vib.* 146 (2) (1991) 243–268.
- [5] J. Becker, O. Fein, M. Maess, L. Gaul, Finite element-based analysis of shunted piezoelectric structures for vibration damping, *Comput. Struct.* 84 (31–32) (2006) 2340–2350.
- [6] J. Ducarne, O. Thomas, J.F. Deu, Placement and dimension optimization of shunted piezoelectric patches for vibration reduction, *J. Sound Vib.* 331 (14) (2012) 3286–3303.
- [7] O. Thomas, J. Ducarne, J.F. Deu, Performance of piezoelectric shunts for vibration reduction, *Smart Mater. Struct.* 21 (1) (2012) 015008.
- [8] G. Caruso, A critical analysis of electric shunt circuits employed in piezoelectric passive vibration damping, *Smart Mater. Struct.* 10 (5) (2001) 1059–1068.
- [9] C.H. Park, Y.H. Kim, H.C. Park, Dynamic formulations of plates with shunted piezoelectric materials, *J. Intell. Mater. Syst. Struct.* 16 (11) (2005) 971–976.
- [10] T. Delpero, A.E. Bergamini, P. Ermanni, Identification of electromechanical parameters in piezoelectric shunt damping and loss factor prediction, *J. Intell. Mater. Syst. Struct.* 24 (3) (2012) 287–298.
- [11] C.M.A. Vasques, Improved passive shunt vibration control of smart piezo-elastic beams using modal piezoelectric transducers with shaped electrodes, *Smart Mater. Struct.* 21 (12) (2012) 125003.
- [12] A. Alaimo, A. Milazzo, C. Orlando, A smart composite-piezoelectric one-dimensional finite element model for vibration damping analysis, *J. Intell. Mater. Syst. Struct.* <http://dx.doi.org/10.1177/1045389X15591380>.
- [13] W. Larbi, J.F. Deu, R. Ohayon, Finite element reduced order model for noise and vibration reduction of double sandwich panels using shunted

- piezoelectric patches, *Appl. Acoust.* <http://dx.doi.org/10.1016/j.apacoust.2015.08.021>.
- [14] J.W. Park, J.H. Han, Sensitivity analysis of damping performances for passive shunted piezoelectrics, *Aerosp. Sci. Technol.* 33 (1) (2014) 16–25.
 - [15] S. Behrens, S.O.R. Moheimani, A.J. Fleming, Multiple mode current flowing passive piezoelectric shunt controller, *J. Sound Vib.* 266 (5) (2003) 929–942.
 - [16] M. Lezgy-Nazargah, P. Vidal, O. Polit, An efficient finite element model for static and dynamic analyses of functionally graded piezoelectric beams, *Compos. Struct.* 104 (2013) 71–84.
 - [17] M. Touratier, An efficient standard plate theory, *Int. J. Eng. Sci.* 29 (8) (1991) 901–916.
 - [18] O. Polit, M. Touratier, High-order triangular sandwich plate finite element for linear and non-linear analyses, *Comput. Methods Appl. Mech. Eng.* 185 (2-4) (2000) 305–324.
 - [19] F. Dau, O. Polit, M. Touratier, An efficient C^1 finite element with continuity requirements for multilayered/sandwich shell structures, *Comput. Struct.* 82 (23-26) (2004) 1889–1899.
 - [20] C. Ossadzow-David, M. Touratier, A multilayered piezoelectric shell theory, *Compos. Sci. Technol.* 64 (13) (2004) 2121–2137.
 - [21] A. Fernandes, J. Pouget, Analytical and numerical approaches to piezoelectric bimorph, *Int. J. Solids Struct.* 40 (17) (2003) 4331–4352.
 - [22] P. Vidal, O. Polit, A family of sinus finite elements for the analysis of rectangular laminated beams, *Compos. Struct.* 84 (1) (2008) 56–72.
 - [23] P. Vidal, O. Polit, A refined sine-based finite element with transverse normal deformation for the analysis of laminated beams under thermo-mechanical loads, *J. Mech. Mater. Struct.* 4 (6) (2009) 1127–1155.
 - [24] S.B. Beheshti-Aval, M. Lezgy-Nazargah, P. Vidal, O. Polit, A refined sinus finite element model for the analysis of piezoelectric-laminated beams, *J. Intell. Mater. Syst. Struct.* 22 (3) (2011) 203–219.
 - [25] H. Kwakernaak, R. Sivan, *Linear Optimal Control Systems*, John Wiley and Sons, New York, 1972.
 - [26] S.B. Beheshti-Aval, S. Shahvaghari-Asl, M. Lezgy-Nazargah, M. Noori, A finite element model based on coupled refined high-order global-local theory for static analysis of electromechanical embedded shear-mode piezoelectric sandwich composite beams with various widths, *Thin Walled Struct.* 72 (2013) 139–163.
 - [27] C.L. Davis, G.A. Lesieutre, A. Modal Strain, Energy approach to the prediction of resistively shunted piezoceramic damping, *J. Sound Vib.* 184 (1) (1995) 129–139.
 - [28] A. Erturk, P.A. Tarazaga, J.R. Farmer, D.J. Inman, Effect of strain nodes and electrode configuration on piezoelectric energy harvesting from cantilevered beams, *J. Vib. Acoust.* 131 (1) (2009) 011010.